12^{th} International Conference on Fracture Mechanics of Concrete and Concrete Structures
FraMCoS-12
B.L.A. Pichler, Ch. Hellmich, P. Preinstorfer (Eds)

https://doi.org/10.21012/FC12.1316
MS05-3:4

MESOSCALE FEM MODEL OF CONCRETE

JAN MAŠEK[*†], **PETR MIARKA**[*†]

[*] Institute of Structural Mechanics,
Brno University of Technology, Veveří 331/95, 602 00 Brno, Czech Republic
e-mail: jan.masek1@vut.cz, petr.miarka@vut.cz

[†] Institute of Physics of Materials,
Czech Academy of Sciences, Žižkova 22, 616 00 Brno, Czech Republic
e-mail: masek@ipm.cz, miarka@ipm.cz

Key words: Meso-scale model, heterogeneous structure, finite element method

Abstract. Heterogeneity of concrete originates in the production process, which consists of bonding aggregates together with a matrix of a binder. The presented meso-scale model can provide the much valuable information about the fracture process at the level of aggregate to cement matrix bond. It therefore aims to describe one of key properties of concrete that is the strain-softening behaviour as a response to mechanical loading. The detail of stress analysis is deeper compared to the discrete models as their description of the inter-particle interaction tends to average out the possibly important stress concentrations. The presented MFEM modelling approach accepts the higher solution costs, relying on modern High-Performance Computing (HPC). In return, a detailed description especially of the stress field and material damage within the material phases and interfaces can be obtained.

1 INTRODUCTION

Concrete is one of the most widely used construction materials worldwide due to its structural versatility, shape flexibility, and long-lasting durability. From a mechanical perspective, concrete is a heterogeneous material, with its variability originating from the manufacturing process, which involves binding aggregates with a binder, typically Portland cement. In classical structural mechanics, however, concrete is often treated as a homogeneous material with mechanical properties defined by standards.

Nevertheless, the inherent heterogeneity becomes evident at smaller scales, where it crucially affects the initiation of damage. At these scales, concrete can be characterized as a multiphase material, with the number of phases depending on the scale being studied. At the aggregate scale, three phases can be distinguished: the aggregates, the cement paste, and the air pores. A fourth phase, representing the bond between the aggregates and the cement paste, known as the interfacial transition zone (ITZ), is also often modeled.

Many approaches have been developed to model material behavior and established constitutive laws, enabling more accurate predictions of stress and subsequent damage. The most widely used material models are typically expressed in tensorial form, based on classical continuum theory. Examples include the Concrete Damage Plasticity Model [7], the Fracture-Plastic Constitutive Model [3], the microplane models, see e.g. [2], as well as phase-field models [11]. These models treat materials as homogeneous at the macroscale, without explicitly accounting for heterogeneity at lower scales.

Meso-scale models provide valuable insights into the fracture process at this scale between the aggregate and the cement matrix. Their main goal is to capture one of the concrete's key properties: strain-softening behavior under tensile loading. Various discrete numerical models, such as Lattice Discrete Particle Models (LDPM), see e.g. [4], are used for similar pur-poses. However, we note that these models dif-fer primarily in their ability to pinpoint the mo-ment of damage initiation, as their treatment of inter-particle interactions tends to average inter-particle stresses - which is an approach deliber-ately chosen to reduce computational demands. This simplified description subsequently asks for remedies on the material model part. Fre-quently, it is necessary to account for nonlin-earity and softening in early loading stages, es-pecially when modeling cyclic fatigue.

In contrast, the MFEM approach accepts higher solution costs by utilizing modern High-Performance Computing (HPC). In exchange, it provides a detailed description, particularly of the stress field and material damage within the material phases and interfaces. See an illustrative stress distribution on a grain surface in Figure 3c. Displayed is the first principal stress, σ_1.

2 MODEL ASSEMBLY PROCESS

To model the heterogeneous structure of a classical concrete material, we first f ocus on the approach to capture the shape and distribution of the aggregates. Figure 1a shows a typical concrete mesostructure containing granite aggregates surrounded by cement matrix. The shape of the aggregates depends on the material and origin of the aggregate material. However, frequently, the aggregates resemble sharp-sided convex polyhedra (e.g. crushed granite or crushed brick recyclate). Without any excessive simplification i s t h erefore p o ssible t o utilize convex polyhedral shapes within numerical models. Figure 1b illustrates that convex polyhedra can be identified i n t h e s h own concrete mesostructure.

Figure 1: a) A typical concrete mesostructure, b) a possible approximation of aggregates by convex polyhedra.

2.1 Generation of aggregate structure

The generation of the mesostructure begins with conducting a tessellation upon a set of generating nodes. A classic Voronoi cell, C_i, contains all domain points, $\mathbf{u}$, that are closer to the respective generating node $\mathbf{x}_i$ than to any other generating node $\mathbf{x}_k$ in the model domain, Ω :

$$C_i = \left\{ \mathbf{u} \in \Omega \;\middle|\; \forall k \neq i \;\; \begin{matrix} ||\mathbf{x}_i - \mathbf{u}|| \\ < ||\mathbf{x}_k - \mathbf{u}|| \end{matrix} \right\}. \quad (1)$$

Unlike that, we utilize the Power diagram variant [1]. The Power diagram is a weighted version of the crude Voronoi tessellation, where each cell, P_i, encompasses all domain points associated with a sphere of radius r_i around its generating node, $\mathbf{x}_i$:

$$P_i = \left\{ \mathbf{u} \in \Omega \;\middle|\; \forall k \neq i \;\; \begin{matrix} ||\mathbf{x}_i - \mathbf{u}||^2 - r_i^2 \\ < \; ||\mathbf{x}_k - \mathbf{u}||^2 - r_k^2 \end{matrix} \right\}. \quad (2)$$

This way, we achieve an uneven distribution of Voronoi cell sizes that approximates a Fuller curve from $d_{\min}$ to d_{max}, see Figure 2a. All the figures in Figure 2 show a 2D illustration of the mesostructure generation process.

The model geometry is created by random sequential placing of nodes into the volume domain of the intended model, Ω. We restrict the mutual distance of the nodes, d, in the range between $d_{\min}$ and $d_{\max}$. The generator starts at the minimum interparticle distance $d = d_{\max}$ and randomly places nodes into the domain, ensuring that that no two nodes are closer than d. After 10^5 of consecutive failed trials, the algorithm

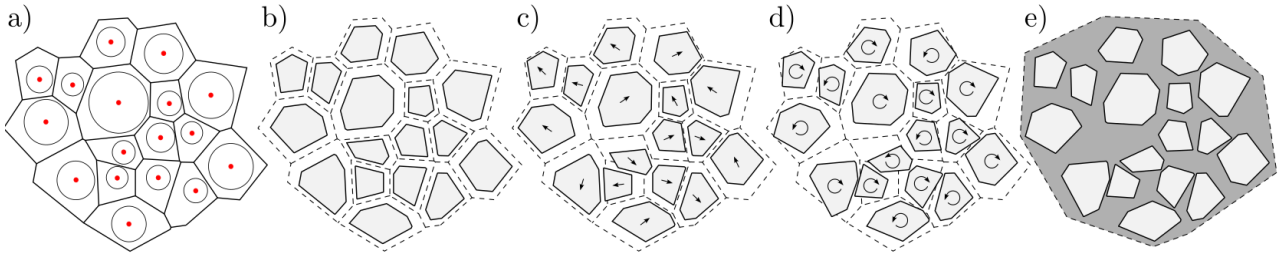

Figure 2: An illustration of the mesostructure generation process: a) Power diagram of the input nodes, b) shrinking the cells (aggregates) towards their center of gravity to create the matrix volume, c) a random translation of the cells, d) random rotation of the cells, e) the resulting mesostructure with aggregates and cement matrix.

decreases d to a next smaller value on the Fuller curve and repeats the process. The generation ends after reaching a target domain saturation, here 95%.

To create the heterogeneous mesostructure resembling a generic concrete, we now shrink the cells towards their respective centres of gravity, creating an intermediate zone that will eventually contain the cement matrix, see Figure 2b. The minimal distance of generating nodes and their radii during the initial node generation reflects this subsequent shrinking so the final grains are of the intended final size. Depending on the expected level of aggregate compacting, the shrinkage may vary from 5% to 50% of grain volume.

To further enrich the structure, we shift each cell randomly within the available surrounding space, see Figure 2c. Lastly, to break the mutual parallelism of cell surfaces, each cell is rotated by a random 3D angle, see Figure 2d. During the process, we ensure that no two cells (grains) collide with each other. This way, a mesostructure resembling that of a concrete material is created, compare Figure 2e to Figure 1b. A 3D illustration of the created structure is presented in Figure 3a. Figure 3b illustrates the aggregate structure in a context of a three-point bending test specimen used in the numerical part that follows.

2.2 Geometry processing and meshing

The described structure can be generated across the exact volume of the intended numerical model or the model can be cut from a greater bulk of the material structure, depending on whether the mesostructure around the model boundaries shall reflect the influence of a formwork or e.g. a specimen cut out of the structure.

The resulting geometry and topology of the aggregate structure is imported into the ANSYS framework, using the PyMAPDL library [6] and volume objects are created according to the topology. For intricate 3D topologies, the mesh generation can constitute a significant portion of the overall computational time. As a result, the default ANSYS APDL mesher was deemed unsuitable due to its lack of efficiency and performance. Instead, we have opted to leverage the highly efficient Gmsh mesh generator [5],

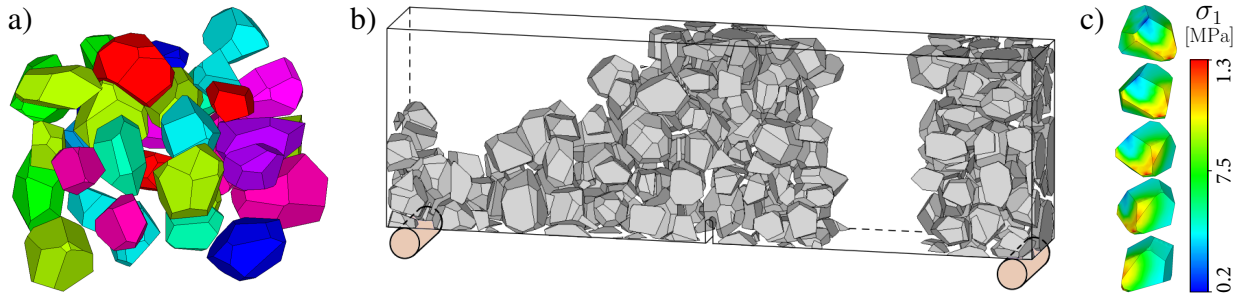

Figure 3: a) A 3D representation of aggregates, b) example of the mesostructure within a notched three-point bending specimen, c) exemplary σ_1 stress field on the surface of an aggregate.

which offers substantial improvements in both speed and versatility. Specifically, we employ the HXT algorithm [8] within the Gmsh library, known for its remarkable efficiency in generating complex 3D meshes.

For the volumetric meshing of the model, we utilize the 20-node hexahedral SOLID186 (elastic analysis) or the CPT216 elements (nonlinear modeling), degenerated into their tetrahedron-degenerated form. This approach is necessary for effectively meshing geometries with complex features, ensuring both accuracy and computational feasibility. It is, however, critical to carefully select an appropriate element size to prevent excessively large stress gradients in the model. Further, to model the possibility of matrix-aggregate separation, the surface of aggregates is covered with INTER204 cohesive elements. For modeling of nonlinear and damage behavior, we utilize variants of the Plasticity Damage Microplane model [12].

3 NUMERICAL EXAMPLE

To preserve natural resources and reduce waste and its storage, the use of crushed bricks as coarse aggregates in concrete is increasingly studied. For bricks, the material properties may vary significantly, see e.g. [10]. In comparison to crushed granite ($E \approx 75$ GPa), the Young's modulus of crushed bricks is reported to vary anywhere between 3.5 GPa and 34 GPa. As for the Poisson ratio, the values may range between 0.12 to 0.29. Depending on the water-to-cement ratio, Young's modulus of the cement matrix may vary between 10 to 35 GPa.

As the stiffness mismatch between aggregates and matrix increases, the stress concentrations grow due to the increasing incompatibility in deformation between the phases. On the other hand, when stiffnesses are comparable, stress is more evenly distributed, possibly reducing the risk of localized failure.

In the presented example, a linear material model for both matrix and aggregate materials is used to study the changes in stress distribution in dependence on the matrix-to-aggregate stiffness ratio, i.e. a heterogeneity parameter, $R_E = E_{\text{mat}}/E_{\text{agg}}$. As stated above, the heterogeneity parameter, R_E, may range roughly between 0.25 (4 times softer matrix) to 5 (5 times softer aggregates).

Obtained maximum normal stresses, σ_x, may be utilized in prediction of fatigue life using Linear Elastic Fracture Mechanics (LEFM). Within the LEFM theory, the uniaxial stress is used to calculate the stress intensity factor, K_I. In the present study, the MFEM model is compared to LEFM stress distribution and therefore, σ_x must be compared.

3.1 Notched three point bending

A standard three-point bending beam test setup is used, encompassing both notched and unnotched variants. The test specimen has a span $S = 240$ mm, depth $D = 80$ mm, thickness $T = 80$ mm, and, in the case of the notched variant, a notch height $a = 0.1D$. The notch is 3 mm wide and its tip is rounded. The numerical model is illustrated in Figure 4.

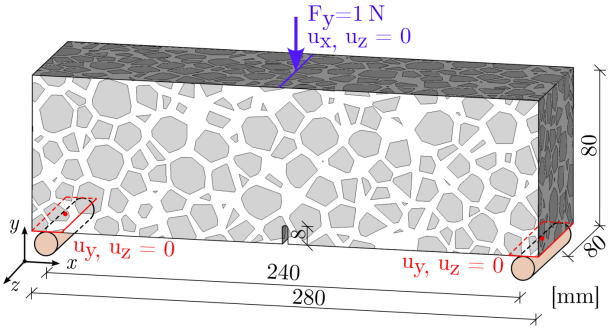

Figure 4: Boundary conditions and dimensions of 3D notched three point bending numerical model.

The boundary conditions for the supports are modeled by creating rigid regions with a width of $S/20$ on the bottom face of the beam (CERIG). Each rigid region is associated with a master node (MASS21), located at the center of gravity of the region, as shown in red in Figure 4. The exact distance between the two master support nodes is set to match the intended beam span S. The boundary conditions applied to the supports include zero displacements in the y- and z-directions (denoted as u_y and u_z),

as well as zero rotations of the supports about the x-axis and zero rotation of the entire model about the y-axis.

The boundary conditions for the top load are modeled similarly. A narrow rigid region is created across the top surface of the model, and a master node is assigned to its center. The loading master node is assigned a vertical force, $\mathrm{F}_y = 1\,\mathrm{N}$, corresponding to a unitary load, while its horizontal displacements u_x and u_z are constrained to zero. Because the numerical model is kept within an elastic regime, the obtained stress field is independent of the actual stiffness values, but rather only on their ratio (a measure of deviation from homogeneity). Due to a constant geometry, the only factor causing a varying stress field is the matrix-to-aggregate stiffness ratio, R_E. If of interest, the elastic analysis allows for scaling the resulting stress fields obtained from the unitary load to the desired load magnitude.

3.2 Execution

To optimize computational efficiency, regions of the model with expected low stress gradients are coarsened, see Figure 5. These areas exhibit minimal variations in stress distribution, allowing for mesh reduction without significant loss of accuracy. Such an approach was verified e.g. in [9].

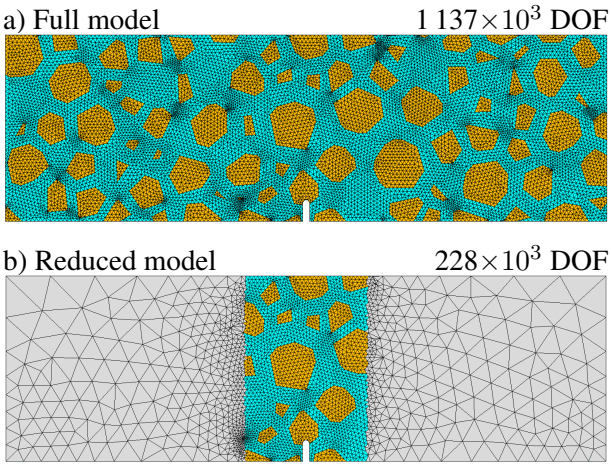

Figure 5: Reducing model complexity by coarsening regions with expected low stress gradients

In this work, without any noticeable loss of precision, computational demands were lowered by modeling and fine-meshing the mesostructure only within the inner 25% of width. In this fine region, maximum element size was set to 1.5 mm. Within the left and right 37% of model width, coarse mesh was used, containing a material with properties averaged between the cement matrix and aggregates. In the coarse region, maximum element size was left free except for the support regions where the maximum element size was restricted to 6 mm.

Using the efficient Gmsh library provides a substantial preprocessing speedup as compared to the ANSYS proprietary mesher. Subsequently, the assembled numerical models are executed using the computational resources of the Czech IT4Innovations National Supercomputing Center. The execution benefits from a massive solution speedup that results from a possible utilization of multiple multiprocessor computational nodes with vast memory and storage resources.

Table 1: FEM Model Comparison

	Full model	Reduced model
Volume Elements	$2\,040\times10^3$	406×10^3
Degrees of Freedom	$1\,137\times10^3$	228×10^3
Gmsh Meshing	15 min	90 sec
ANSYS Solution	10 min	1.5 min
RAM Required	148 GB	41 GB
Energy Used	0.597 kWh	0.107 kWh

Table 1 presents a comparison between a full and a reduced finite element model in terms of computational efficiency, resource requirements, and energy consumption. The table lists the number of volume elements and degrees of freedom (DOFs) for each model, as well as the meshing time in Gmsh, the ANSYS solution time using 8 computation nodes (totaling 288 cores - $8 \times 2 \times 36$ cores of Intel Cascade Lake 6240), the RAM required for in-core solution of the FEM problem, and the total energy used during computation.

The full model consists of 2.04 million volume elements and approximately 1.137 million DOFs, requiring 15 minutes for meshing, 148

GB of RAM, and 16 minutes for the solution, consuming 0.597 kWh of energy. In contrast, the reduced model contains 406 thousand volume elements and 228 thousand DOFs, significantly reducing the computational cost with a meshing time of 90 seconds, a RAM requirement of 41 GB, and an ANSYS solution time of only 3 minutes, consuming 0.107 kWh.

3.3 Stress field analysis

To evaluate the stress field in the models, we extract stress values from multiple parallel cross-sections along the specimen, see Figure 6. If the cross-section positions are sufficiently close such that they represent material regions under a similar mechanical load, we can treat the stress values as though they come from a single cross-section of a defined thickness. To minimize information loss, we propose breaking down the cross-section height into several thin layers, each of which has histograms of stress values. These histograms are then placed according to their respective layers, creating a comprehensive display of the stress distribution within the model's volume.

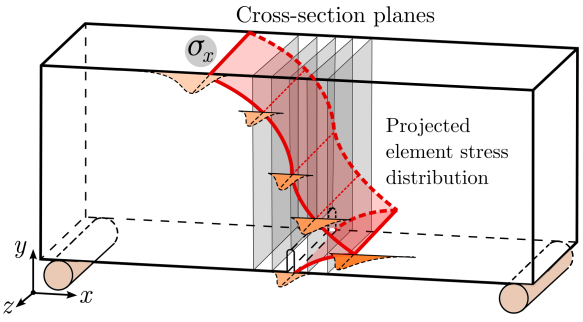

Figure 6: Notched three point bending numerical model.

This method ensures that no information is lost or averaged out. The resulting display preserves detailed information about both the stress extremes and the overall stress distribution. The results presented below were acquired within 10 equidistant cross-sections equidistantly spread across the notch width, extracted from 20 numerical models with unique aggregate structures.

3.3.1 Normal stress results

In what follows, we present a comparison between the analytical LEFM solution for the midspan normal stress field, $\sigma_{x_{\mathrm{LEFM}}}$, in a homogeneous material and the σ_{MFEM} values obtained from the numerical model, as described in Section 3.3. It is important to note that the $\sigma_{x_{\mathrm{LEFM}}}$ values are computed for a sharp notch tip, and a direct comparison is not strictly intended. The material properties in the MFEM model vary according to the heterogeneity parameter, ranging from $R_E = 0.1$ to $R_E = 10$, while the Poisson ratio remains fixed at $\nu = 0.2$ for all materials. The aggregate structure is generated to resemble a distribution of aggregate sizes between 2 and 16 mm.

Figures 7 and 8 show the obtained results from both numerical MFEM and analytical LEFM models. The MFEM stress values are displayed in a relative histogram for a fine array of layers across the specimen height. Therefore in each layer, dark red are the most frequent stress values and towards dark blue, the frequency of occurrence decreases.

It can be concluded from the presented results in Figures 7 and 8, that there is a good match between the expected distribution of normal stresses and the numerical model for a homogeneous material ($R_E = 1$). When stiffnesses are comparable ($R_E \approx 1$), the strains in the matrix and aggregates are compatible, leading to a smoother stress distribution. However, as the heterogeneity gets more pronounced in either way, the normal stress distribution within matrix and aggregates changes. In the case of matrix being softer than the aggregates (i.e. $R_E < 1$), the stress peaks within the matrix tend to get smeared as the matrix deforms more easily while transferring the load from aggregate to aggregate. However, in limit, the matrix still remains responsible for ensuring the overall equilibrium and therefore the stress it conducts cannot approach to zero. In the case of aggregates being softer than the matrix (i.e. $R_E > 1$), stiffer matrix attracts more stress due to its higher resistance to deformation. By de-

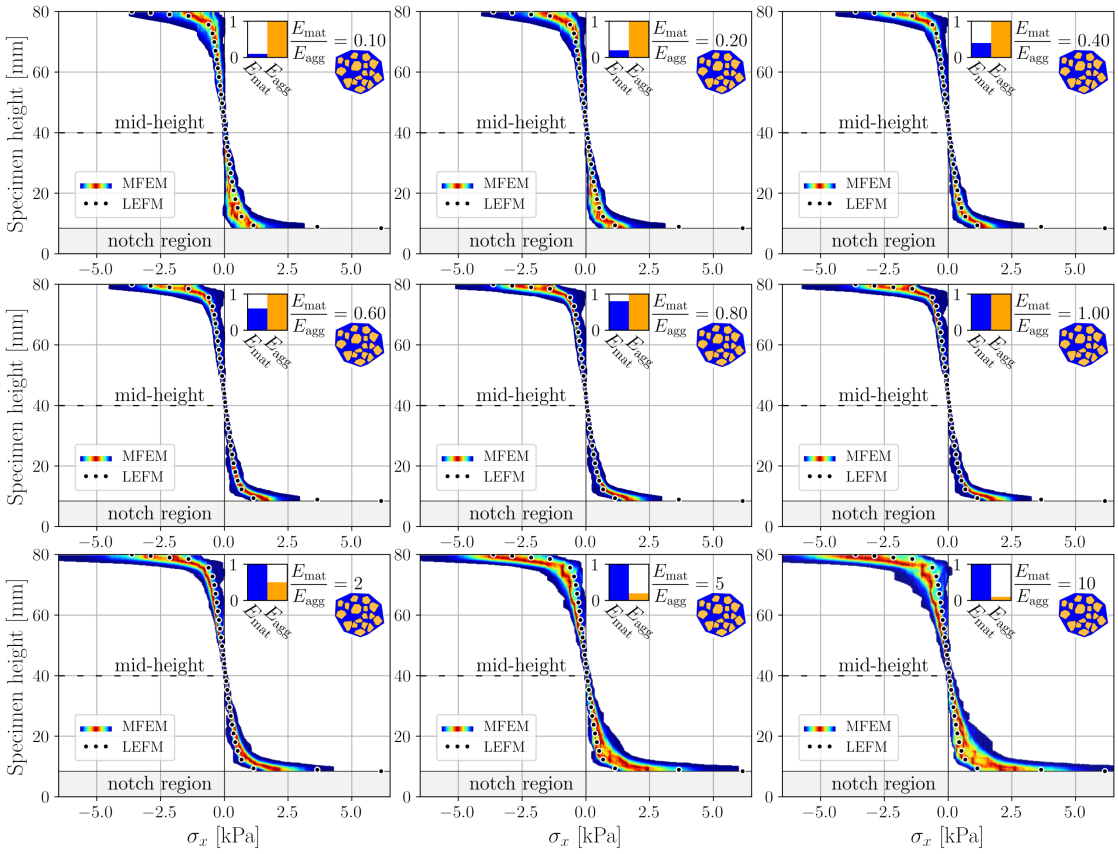

Figure 7: Matrix normal stress within the notch region in dependence on the heterogeneity parameter, R_E.

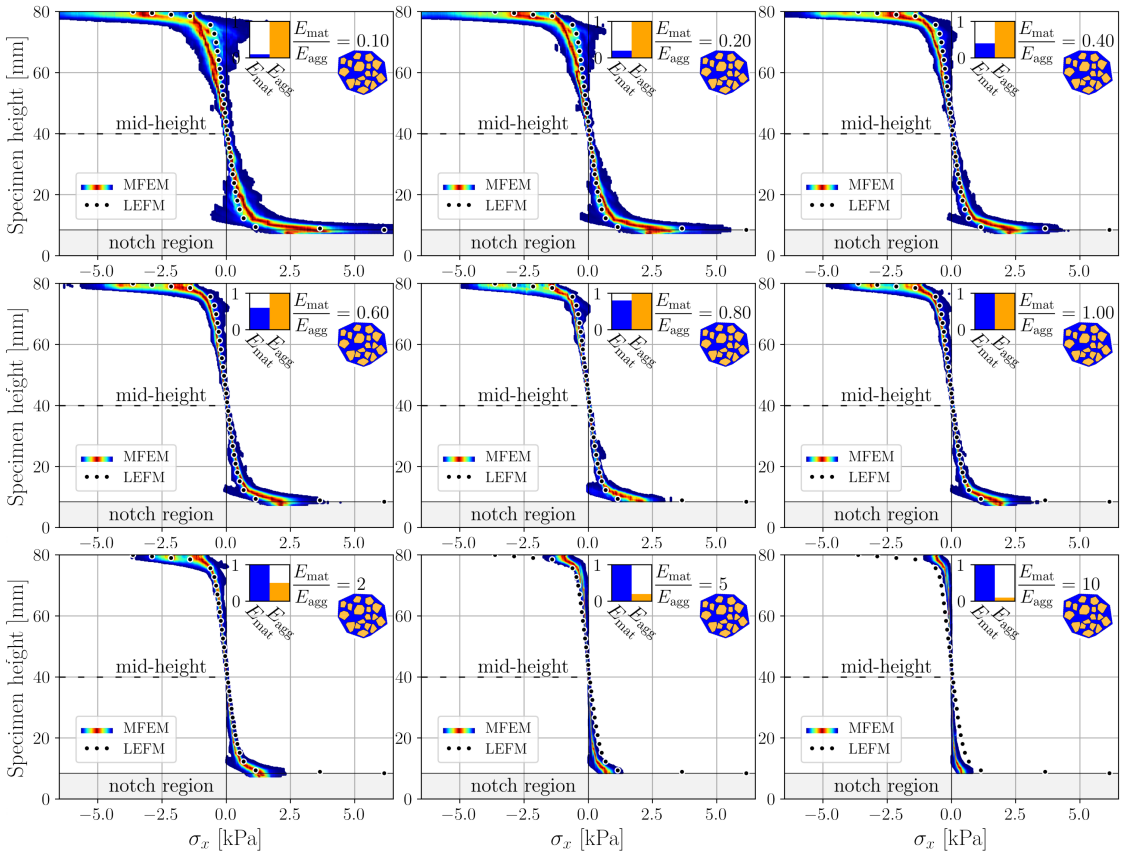

Figure 8: Aggregate normal stress within the notch region in dependence on the heterogeneity parameter, R_E.

creasing their stiffness, aggregates start to lose the ability to transfer the stress across the composite due to their easy deformation. To retain equilibrium, an increasing amount of stress has to be conducted over the cement matrix. In limit, the composite becomes a cement matrix filled with void inclusions.

This phenomenon is further illustrated in Figure 9 by showing maximum normed normal stress quantiles, $\overline{\sigma}_{x,\max}(q)$:

$$\overline{\sigma}_{x,\max}(q) = \frac{\sigma_{x,\max,\text{hetero}}(q)}{\sigma_{x,\max,\text{homo}}(q)}\,, \tag{3}$$

where $\sigma_{x,\max,\text{hetero}}(q)$ is the qth quantile of maximum normal stress within a given heterogeneous material and $\sigma_{x,\max,\text{homo}}(q)$ is the qth quantile of maximum normal stress within a homogeneous material ($R_E = 1$).

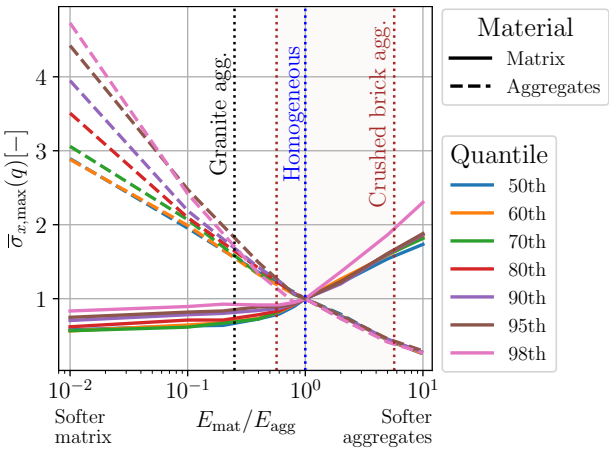

Figure 9: Normed normal stress quantiles $\overline{\sigma}_{x,\max}(q)$.

From the presented stress analysis, it can be concluded that utilization of aggregate materials softer ($R_E > 1$) than the cement matrix leads to increased stress concentrations within the matrix material. Within the range of crushed brick material properties, the increase of the maximum matrix stress may reach up to $2\times$ compared to crushed granite aggregates.

4 CONCLUSIONS

In the presented contribution, a Mesoscale Finite Element Model (MFEM) of concrete is presented. The developed model captures the concrete structure in a finer scale than the LDPM models. It allows to study and understand the mechanical phenomena within concrete on a finer scale. Supported by today's high performance computing possibilities, the modeling approach captures the aggregate structure of concrete in detail, allowing for a statistical evaluation across many model realizations.

In the presented contribution, a statistical analysis of normal stress within three-point bending test specimen was presented. The focus was put on the influence of stiffness heterogeneity between cement matrix and used aggregate material. From the presented results, it can be concluded that using materials with Young's modulus lower than cement matrix leads to severely increased stress concentrations within the matrix material, possibly increasing the risk of fatigue damage initiation. However, the initially uniaxial stress will be distorted due to the heterogeneous meso-structure. This will create a necessity to account for multiaxial stress states in future damage initiation studies and eventually, to develop a specific criteria for fracture.

ACKNOWLEDGEMENT

This contribution was created as a part of project No. CZ.02.01.01/00/22_008/0004631 Materials and technologies for sustainable development within the OP JAK Program financed by the European Union and from the state budget of the Czech Republic.

This work was supported by the Ministry of Education, Youth and Sports of the Czech Republic through the e-INFRA CZ (ID:90254).

DATA AVAILABILITY

The data used in this study is available at: https://doi.org/10.5281/zenodo.14280526 .

REFERENCES

[1] Franz Aurenhammer. Power diagrams: properties, algorithms and applications. *SIAM Journal on Computing*, 16(1):78–96, 1987.

[2] Ferhun C Caner and Zdeněk P Bažant. Microplane model m7 for plain concrete. i: Formulation. *Journal of Engineering Mechanics*, 139(12):1714–1723, 2013.

[3] Jan Červenka and Vassilis K Papanikolaou. Three dimensional combined fracture–plastic material model for concrete. *International journal of plasticity*, 24(12):2192–2220, 2008.

[4] Gianluca Cusatis, Daniele Pelessone, and Andrea Mencarelli. Lattice discrete particle model (ldpm) for failure behavior of concrete. i: Theory. *Cement and Concrete Composites*, 33(9):881–890, 2011.

[5] Christophe Geuzaine and Jean-François Remacle. Gmsh: A 3-d finite element mesh generator with built-in pre-and post-processing facilities. *International journal for numerical methods in engineering*, 79(11):1309–1331, 2009.

[6] Alexander Kaszynski. pyansys: Pythonic interface to MAPDL, November 2021.

[7] Jeeho Lee and Gregory L Fenves. Plastic-damage model for cyclic loading of concrete structures. *Journal of engineering mechanics*, 124(8):892–900, 1998.

[8] Célestin Marot, Jeanne Pellerin, and Jean-François Remacle. One machine, one minute, three billion tetrahedra. *International Journal for Numerical Methods in Engineering*, 117(9):967–990, 2019.

[9] Jan Mašek, Josef Květoň, and Jan Eliáš. Adaptive discretization refinement for discrete models of coupled mechanics and mass transport in concrete. *Construction and Building Materials*, 395:132243, 2023.

[10] SP Narayanan and M Sirajuddin. Properties of brick masonry for fe modeling. *American Journal of Engineering Research*, 1(2013):6–11, 2013.

[11] Zhen-Jun Yang, Bei-Bei Li, and Jian-Ying Wu. X-ray computed tomography images based phase-field modeling of mesoscopic failure in concrete. *Engineering Fracture Mechanics*, 208:151–170, 2019.

[12] Imadeddin Zreid and Michael Kaliske. A gradient enhanced plasticity–damage microplane model for concrete. *Computational Mechanics*, 62(5):1239–1257, 2018.